Mesoscopic scale simulation of dislocation dynamics in fcc metals: Principles and applications

M Verdier†‖, M Fivel‡ and I Groma§

† LTPCM Domaine Universitaire-BP 75 38402 St Martin d'Hères Cedex, France
‡ GPM2 Domaine Universitaire-BP 46 38402 St Martin d'Hères Cedex, France
§ Institute for General Physics, Eotvos University, H-1445 Muzeum krt. 6–8, Budapest VIII, POB 323, Hungary

This paper is dedicated to Gilles Canova, who initiated and participated in the development of the numerical simulations presented in this paper.

Abstract. This paper reviews the methods and techniques developed to simulate dislocation dynamics on a mesoscopic scale. Attention is given to techniques of acceleration and to the implementation of special boundary conditions. Typical results concerning the deformation of a bulk crystal, the effect of image forces and the combination with a finite-element code to simulate the indentation test are presented. The limits and future development of each application are discussed.

1. Introduction

Dislocations are the vector for plastic deformation in crystalline solids and in materials where the long-range interactions between dislocations dominates, as in, for example, most face-centred-cubic (fcc) metals where the emergence and evolution of a heterogeneous microstructure of dislocations governs mechanical properties.

At the mesoscopic scale, i.e. the scale between the atomic level and the macroscopic level of the mechanical properties, the basic entity is the dislocation line. The dislocations interact through a long-range stress field (in $1/r$), and as a non-conservative N-body problem it is difficult to treat analytically. Therefore, with the aim of studying the self-organizing patterns of the dislocation structure and their influence on the mechanical properties of a single crystal, a framework for a three-dimensional (3D) numerical simulation of dislocations on a mesoscopic scale has been developed in the past few years [1]. This work has recently been reviewed [2].

A different version of this simulation has recently been developed to test an acceleration scheme required to reach some larger strain [3]. Moreover, to study physical problems where a high density of dislocations in the volume simulated is not required, such as the role of interfaces and the indentation test, some complex boundary conditions have been developed and implemented [4–6]. In the present paper, we first briefly review the key elements for such simulations, emphasizing the different techniques that we have developed. Then, we present the different boundary conditions developed in this simulation for the case of

‖ Present address: Los Alamos Nal Lab, CMS, MS:765, Los Alamos, NM 87545, USA.

modelling the behaviour of bulk crystal, and for situations where a complex boundary is required, such as surfaces taking into account image forces or indentation of a crystal. In the last part, typical results concerning each case are presented and the limit of the various methods are discussed.

2. General frame

2.1. Discretization of space and dislocations

The computer model was developed in the same scheme as detailed in [1]. The crystal considered in this work has a face-centred-cubic structure (fcc). Dislocations are introduced as linear discontinuities in an isotropic elastic continuum represented by a cube. A lattice homothetic to a fcc lattice is superimposed on the cube: the length scale of this mesoscopic network is deduced from experimental observations by Essmann and Mughrabi [7] in Cu, where these authors observed a critical annihilation distance around 26 Å and 500 Å, respectively, for edge and screw dipoles. Therefore, the minimum distance where two dislocations can coexist, 26 Å, is taken as the unit length of the lattice. This length is bigger than the core radius of the dislocation (3–10 Å) and allows the use of elastic expressions for the stress interaction between dislocations without the nonlinearity problems related to their core structures.

The dislocation considered in the simulation of fcc metals are all glissile, therefore six Burgers vectors of $\langle 110 \rangle$ type are used. Dislocation lines are discretized into straight segments of pure edge and screw characters as proposed by Devincre and Condat [8], connected on the node of the mesoscopic lattice. Each screw segment, whose line vector is aligned along $\langle 110 \rangle$, can glide in the two (111) planes associated with the $\langle 110 \rangle$ direction along a $\langle 211 \rangle$ direction. This describes simple glide and cross-slip geometry of a screw dislocation. The edge segments have line vectors along the $\langle 211 \rangle$ direction and can glide only along the orthogonal $\langle 110 \rangle$ direction associated, the climb being not implemented for simulation of plasticity of crystal at room temperature. The 12 glissile systems are enumerated in table 1 with the Schmid and Boas notation.

Table 1. List of vectors and system used in the simulation for fcc metals.

	System											
	1	2	3	4	5	6	7	8	9	10	11	12
Edge	$\bar{1}01$	$\bar{1}01$	011	011	$\bar{1}10$	$\bar{1}10$	110	110	$01\bar{1}$	$01\bar{1}$	101	101
Screw	$\bar{1}2\bar{1}$	121	$2\bar{1}1$	$21\bar{1}$	$11\bar{2}$	$\bar{1}\bar{1}2$	$1\bar{1}2$	$\bar{1}1\bar{2}$	$2\bar{1}1$	211	$\bar{1}21$	$12\bar{1}$
Normal	111	$1\bar{1}1$	$\bar{1}\bar{1}1$	$1\bar{1}1$	111	$11\bar{1}$	$1\bar{1}1$	$1\bar{1}\bar{1}$	111	$\bar{1}11$	$11\bar{1}$	$1\bar{1}\bar{1}$
Schmid and Boas	B4	D4	C1	D1	B5	C5	D6	A6	B2	A2	C3	A3

2.2. Effective stress

The movement of the dislocation line is made of a succession of motion of each straight segment, applying a molecular dynamics scheme. The kinetics of motion of a straight segment depends upon the local effective stress and the line tension. The local effective stress is a sum of several contributions:

(i) a threshold stress defined by the friction shear stress of the crystal (Peierls stress). For Cu, one estimates $\tau_{\text{Peierls}} = 3 \times 10^{-5}$ G = 1.26 MPa, where G is the shear modulus;

(ii) the internal stress field due to the dislocations $((\sigma_{int}))$. This computation is based on the elastic stress field created by a finite dislocation segment, using DeWit's formula [9] modified by Devincre and Condat [8]. Because of the long-range interaction of dislocations $(1/r)$, no cut-off radius can be introduced. This implies computing N^2 interactions (N being the number of segments) for each time step. We have developed a method to decrease this number of computations detailed later;

(iii) the external stress tensor $((\sigma_{ext}))$. For example, the macroscopic tensor of an uniaxial tensile stress which is applied homogeneously in the cube, or the local stress coming from an indenter; and

(iv) the image force tensor $((\sigma_{im}))$ taking into account free surfaces.

The effective resolved shear stress τ^* on a segment of Burgers vector $\boldsymbol{b}$ and line vector $\boldsymbol{l}$, is calculated using the Peach–Koehler formula

$$\tau = [[((\sigma_{int})) + ((\sigma_{ext})) + ((\sigma_{im}))] \cdot \boldsymbol{b}]\hat{\boldsymbol{l}}. \tag{1}$$

And taking into account the friction shear stress

$$\tau^* = \tau - \text{sign}(\tau) \cdot \tau_{Peierls}. \tag{2}$$

2.3. Line tension

The line tension, or self stress of the dislocation line, is calculated either from the gradient of the self-energy due to virtual displacements as described in [8] or from the local radius of curvature of the dislocation line. This latter approach leads to a less squared shape of the dislocation loop produced by the Frank Read mechanism of dislocation multiplication because it is less dependent on edge-screw discretization of the dislocation line. Letting R be the local curvature radius of a dislocation line under equilibrium, one has according to Cottrell [10]

$$|\tau_{line\ tension}| = \frac{\alpha G b}{R} \tag{3}$$

where $\alpha = 0.63$ is obtained from the experimental observations of the curvature radius of dislocation lines by Mughrabi [11].

2.4. Dynamic of dislocations

Evolution of the dislocation configuration is based on a molecular dynamics scheme; the time step of the simulation is typically set around 10^{-9} s, which allows for a permanent regime for the speed v of the dislocation segments. Then, v obeys a Newtonian-type law

$$v = \tau^* \frac{b}{B} \tag{4}$$

where B is a viscous drag coefficient due to interactions with phonons at room temperature ($B = 1.5 \times 10^{-5}$ Pa s for Cu) [12]. To take into account the dynamics of segments of different speeds, the time step is limited to the order of magnitude of 10^{-9} s, and an arbitrary speed limit is set to 100 m s^{-1}.

2.5. Core effects

To take into account local properties related to the core of the dislocation, such as the cross-slip of screw dislocations, the annihilation/recombination of lines, and sessile junction formations, one has to add some rules to the model.

The cross-slip mechanism of screw segments is based on a stochastic test using the following probability per unit of time

$$P = \beta \frac{L}{L_0} \frac{\delta t}{\delta t_0} \exp\left(V \cdot \frac{[\tau^* - \tau_{\text{III}}]}{kT}\right) \tag{5}$$

where τ_{III} is the resolved shear stress at the onset of stage III of plastic deformation, V is the activation volume, k is the Boltzmann constant, β is a normalizing coefficient, and L_0 and δt_0 are respectively references to length and time. According to the work of Bonneville *et al* [13] concerning Cu crystals, $V = 300\, b^3$ and the probability P is set to one at room temperature when a $L_0 = 1\,\mu\text{m}$ screw dislocation under a resolved shear stress $\tau^* = \tau_{\text{III}}$ is at a critical distance on a parallel plane (500 Å for Cu) of an opposite Burgers vector screw dislocation.

The rules concerning annihilation and recombination of segments are naturally done on the lattice using a sign convention of the orientation of the dislocation lines. For non-coplanar crossing of dislocations, only attractive sessile junction formation is taken into account based on a line energy minimization criterion

$$b_1^2 + b_2^2 < (b_1 + b_2)^2 \tag{6}$$

i.e. the segments of b_1 and b_2 Burgers vector are immobilized when this condition is true. Sessile junctions are destroyed when the resolved shear stress on the immobilized segments exceeds a threshold value τ_j, set to 12.5 MPa based on comparison with the forest hardening model [14].

3. Acceleration methods

For N segments in the simulation, the total number of interactions required to compute $((\sigma_{\text{int}}))$ per time step is equal to $N^2 - N$. To reduce this number, we have used the assumption that the time and space variations of the long distance stress field are small. Therefore, the cube is subdivided into $(M \times M \times M)$ boxes, as shown in figure 1.
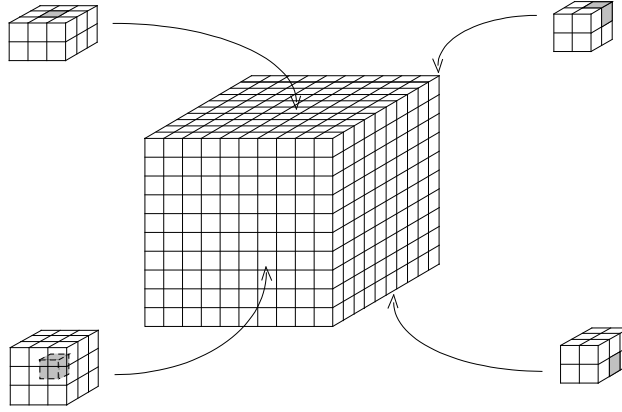

Figure 1. Scheme of the box system used for the long-distance stress field calculation.

For each box, we define the short distance volume as being the box itself and its first neighbours, and the long distance the remaining boxes. Without any approximation, at any segment inside a sub-box S where $((\sigma_{\text{int}}))$ needs to be computed can be written as

$$((\sigma_{\text{int}}))_{\text{segment}} = ((\sigma_{\text{SD}}))_{\text{segment}} + ((\sigma_{\text{LD}}))_{\text{segment}} \tag{7}$$

where $((\sigma_{SD}))$ and $((\sigma_{LD}))$ are the short-distance and long-distance stress fields, respectively. The first assumption is that the long distance stress contribution varies little in the volume of the box. It is taken as constant and calculated at the centre I of the box. The variation of the long-distance stress field is considered to have a long wavelength compared to the half size of the box

$$((\sigma_{int}))_{segment} \approx ((\sigma_{SD}))_{segment} + ((\sigma_{LD}))_{centre\ I}. \tag{8}$$

The second approximation is that $((\sigma_{LD}))_{centre\ I}$ is not updated every time step as $((\sigma_{SD}))_{segment}$ but with a period f.

The total number of interactions for N segments to be computed with this method averaging on all M^3 boxes (in the volume with 26 first neighbours, or less when close to the surface, figure 1) is per time step

$$c(M, f) = \frac{N}{M^3}\left[\frac{1}{f}(M^6 - 27M^3 + 54M^2 - 36M + 8) + 27(N-1) - 54\frac{(N-1)}{M}\right.$$
$$\left. + 36\frac{(N-1)}{M^2} - 8\frac{(N-1)}{M^3}\right]. \tag{9}$$

The efficiency of the method, $c(M, f)/(N^2 - N)$, is plotted in figure 2 for different number of segments. For 50 000 segments with more than $(15 \times 15 \times 15)$ boxes, a minimum factor improvement between five and ten (for f greater than 20 time steps) can be achieved.
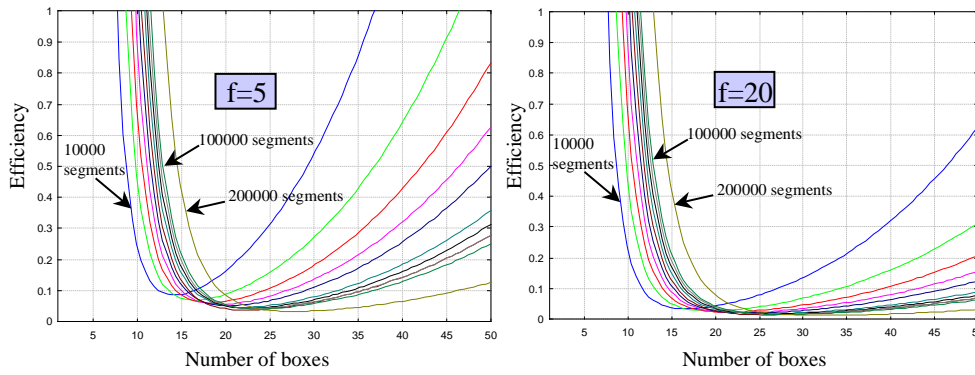

Figure 2. Efficiency of the box method for different updating period f and different number of segments.

The error due to the approximation by assuming a homogenous long-distance stress field within a box is illustrated in figure 3. $((\sigma_{LD}))$ has been calculated along 50 points P on a (111) diagonal of a box and compared to the value at its centre I. A relative error ε_r is defined as

$$\varepsilon_r = \sum \frac{(|\sigma_{LD}^i(P) - \sigma_{LD}^i(I)|)}{\max_k(\sigma_{int}^k(P))} \tag{10}$$

where σ^j is the j component of the $((\sigma))$ tensor written in vectorial notation ($j = 1, 6$). In figure 3, the relative errors have been averaged for the set of points P. The configuration used is obtained after a tensile deformation of a 15 μm simulation cube along [111] and contains 50 079 segments (dislocation density $\rho = 5 \times 10^{12}$ m^{-2}, see for example figure 6).

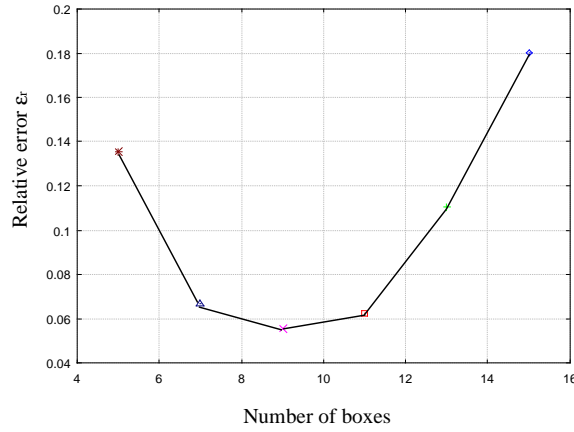**Figure 3.** Averaged relative error introduced by the box method against the number of box (M) per side on the cube.
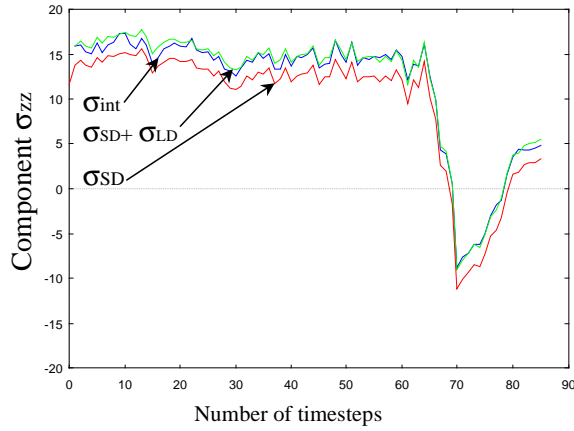

Figure 4. Evolution of σ_{zz} during several simulation steps, σ_{zz} is computed without any approximation (σ_{int}), with the box method ($\sigma_{LD} + \sigma_{SD}$), with a cut-off radius (σ_{SD}). The 15 μm simulated cube has 50 000 segments.

The curve in figure 3 presents a minimum due to the fact that for a small number of boxes, the volume of each box is important, and the long-distance field is not homogenous within a box. For a large number of boxes, the nearest segments belonging to the long-distance volume are too close and an error is introduced by computing their stress field in the centre I instead of P.

An optimum number of boxes between 8^3 to 11^3 boxes was obtained, minimizing the relative error ε_r (10), with a relative error of less than 10%.

The error introduced by the update period is more difficult to evaluate: it strongly depends on the type of mechanical test simulated, the dislocation density and the time step used, factors that would determine the evolution kinetics of a given configuration. However, in figure 4 we have compared the evolution of σ_{zz} of ((σ_{int})) against the number of simulation time steps, calculated with and without the box method. In the case of the calculation with the box method, we use $M = 11$ and $f = 20$ steps. The initial configuration is a cube
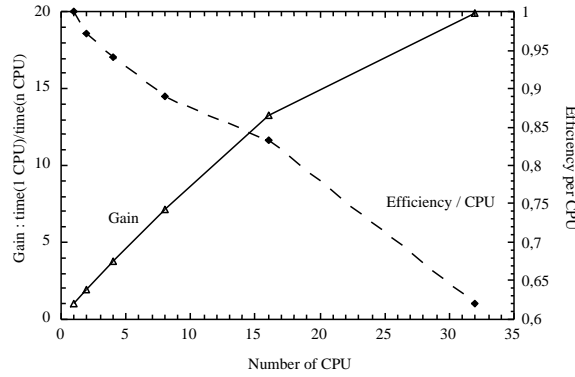
Figure 5. Gain and efficiency per processor for the stress calculation on a (T3D) computer against the number of parallel processors.

of 15 μm size, with 50 000 segments obtained after a macroscopic strain $\varepsilon = 1.5 \times 10^{-4}$ pulled along the z-axis at a strain rate of 50 s^{-1}. For comparison, the component σ_{zz} of the short distance stress $((\sigma_{SD}))$ is also reported: it would correspond to internal stress if a cut-off radius was introduced instead of the box method.

In this figure, it can be seen that using the box method with an update period $f = 20$ steps gives results very close to the exact solution. Moreover, the difference of several MPa between $((\sigma_{SD}))$ and $((\sigma_{int}))$ confirms the need to take the long-distance field stress into account.

In conclusion, this simple box method does not remove the N^2 character of computation required for local interactions. It allows, however, for a computational gain between two and ten times with a relatively small error in the internal stress evaluation.

In order to reduce the user computation time, we have developed a parallel version of the code running on different computers using the parallel virtual machine (PVM) library. Only computation of the resolved shear stress on each segment using the box method has been parallelized, since the part of the code in charge of configuration updates through the segment displacements and is too complex to be easily made parallel. The scheme we have adopted is to spread the internal stress calculation amongst different processors, being helped by the natural subdivision of the box method. Figure 5 illustrates the gain for one internal stress computation and the efficiency per processor against the number of processors, on a Cray T3D for a configuration of 20 000 segments. For such a simulation, the compromise is balance between the time spent for the transfer of the configuration to each processor, and the time spent computing the stress field. Therefore, a maximum number of processors used on this type of machine is on the order of eight, for which the efficiency is 90%. This gain represents the gain only for the stress computation, and it has to be divided roughly by two for the whole simulation, because the configuration update takes around 50% of the time for 20 000 segments when the whole simulation is executed on a single processor.

4. Boundary conditions

Depending on the type of problem studied, different boundary conditions have been developed. We review the different methods used for the simulation of a bulk crystal.
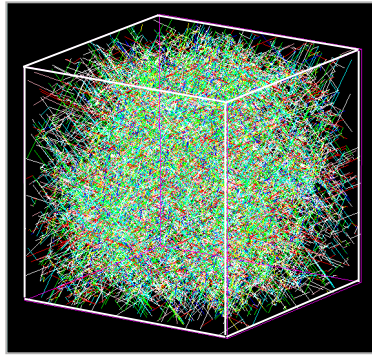
a) (15µm large cube)
$\rho = 9,6.10^{12} \text{ m}^{-2}$
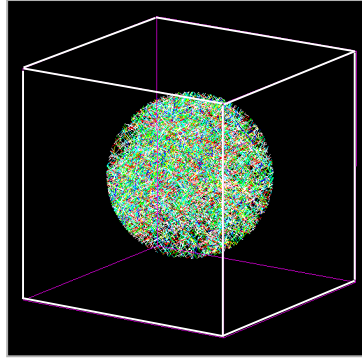
b) (5µm radius sphere)
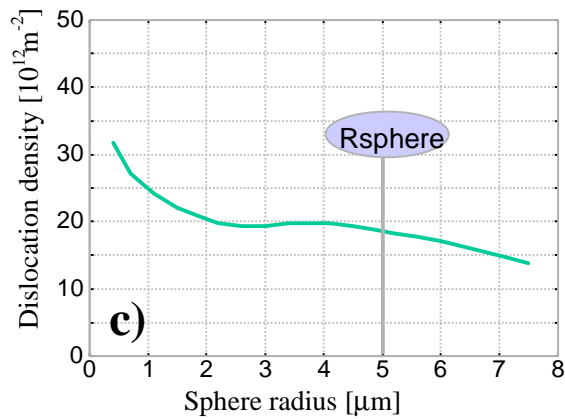$\rho = 18,7.10^{12} \text{ m}^{-2}$

Figure 6. (a) Whole deformed microstructure of 82 270 segments, dislocation density in the 15 μm cube: $\rho = 9.6 \times 10^{12}$ m^{-2}; in the sphere (b) $\rho = 18.7 \times 10^{12}$ m^{-2}. (c) Dislocation density against sphere radius R.

4.1. Bulk crystal simulation

The primary goal for this type of simulation of plastic deformation is to obtain features of the dislocation structure of a bulk single crystal. Therefore, a minimum cube size is 15 μm^3: for dislocation density around 10^{13} m^{-2} which are achievable by simulation in such a volume, the size of an emergent self-organized structure of dislocations should be of several microns diameter. This relatively small volume prohibits the use of real free surface: the images forces from one single surface would have an action to a depth of 4 μm in the cube (cf section 5 of this paper) [6].

Moreover, whatever the sort of boundary (free, periodic, ...) used to simulate a bulk crystal, their effect is not clear. Therefore, for the sake of simplicity, we simulate a cube but only the dislocations inside a sphere are taken into account in terms of data recorded (plastic deformation, density, ...). The choice of a sphere also has the advantage that it

does not favour any crystallographic direction in the process of cutting the segments as they touch the boundary. This sphere lies far enough from the sides of the cube, so that their artifact does not affect too much the content of the sphere. As can be seen in figure 6(a), the dislocation density near the sides of the simulated cube is smaller than towards the centre.

Figure 6(c) shows, for this configuration, evolution of the dislocation density in a sphere with different radii. The effect of the surfaces is seen for a radius greater than 5 μm; the dislocation density is constant in the 4–5 μm range.

4.2. Free surfaces

The use of an elastic continuum as a framework for the simulation allows the use of the principle of elastic field 'superimposition': as described by van-der-Giessen and Needlemann in two dimensions [15], it consists of superimposing both elastic fields from the dislocations and from the boundary, figure 7. For the special case of image forces from a free surface, the use of a finite element code is not compulsory: owing to Boussinesq linear operators [16], an analytical solution exists to determine the elastic field in a half-space volume due to a point load at its flat surface.
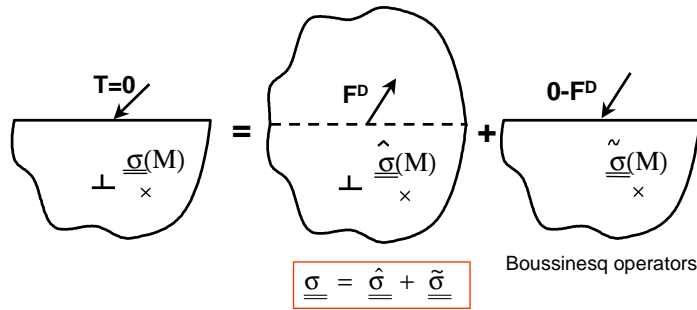

Figure 7. Scheme of the Boussinesq problem applied to a free surface.

Let X' be a point on a surface of a half space where force F is applied, then the elastic tensor in the volume at a point X is

$$\sigma_{ij}(X) = B_{ijk}(X, X')F_k(X') \tag{11}$$

where B is the Boussinesq operator [16]. The method is described in [6] and is in good agreement with the analytical solution of Gosling and Willis for a dislocation loop [17]. An extension of this method can be developed for the case of two free surfaces in order to simulate a free standing thin film [4]. The principle is shown in figure 8.

The problem of image forces of dislocations in this problem is decomposed into two sub-problems:

(i) the image forces F_d and $F_{d'}$ coming from the dislocations in the volume are calculated on the two surfaces (S and S', respectively) as if the dislocations were in an infinite elastic medium. However, reintroduction of the force F_d on the surface S through the Boussinesq operator will create a force F_B' on the surface S' (and also a force F_B on S from the reintroduction of F_d' on S').

(ii) the equilibrium of the surfaces is then obtained by applying the force $-(F_d - F_B)$ on S and $-(F_d' - F_B')$ on S'. The image forces in the volume are then computed using the Boussinesq operator on those two forces.
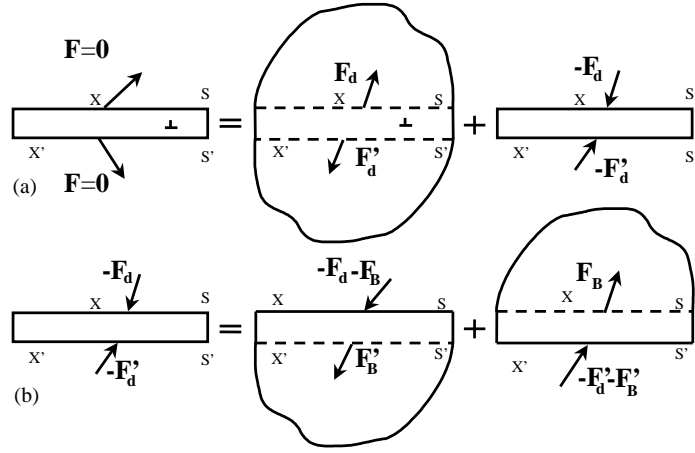
Figure 8. Scheme of the film free surface problem. (a) Superimposition of two elastic problems. (b) Reintroduction of image forces using the Boussinesq method.

4.3. Complex boundary conditions

More complex boundary conditions such as the one occurring during an indentation test can be treated following the same decomposition as described for thin films. However, because the Boussinesq operators deal only with forces of plane loaded surfaces, the use of a finite-element code is required for this more complex boundary condition, as shown in figure 9.
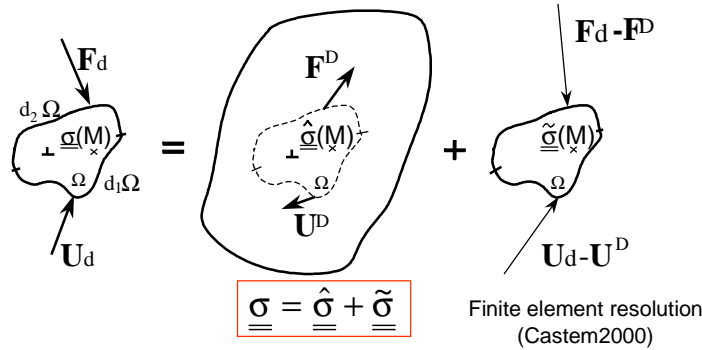

Figure 9. Scheme of dislocations and complex boundary problem in a finite volume Ω, where displacements U_d and forces F_d are imposed (see text).

The finite volume Ω contains some dislocations, an external force F_d is applied on a boundary $\partial\Omega_1$ and a displacement U_d on a boundary $\partial\Omega_2$. The stress field $((\sigma))$ that has to be applied to the dislocations is the sum of $((\sigma_D))$ and $((\sigma_{diff}))$:

(i) $((\sigma_D))$ is the stress field of the dislocations as if they were in an infinite medium (no free surfaces), which in the simulation is $((\sigma_{int}))$. However, $((\sigma_D))$ creates on the boundaries $\partial\Omega_1$ some forces $F^D = ((\sigma_{int})) \cdot n$ (n is normal of $\partial\Omega_1$), and some displacements U^D on $\partial\Omega_2$.

(ii) $((\sigma_{\text{diff}}))$ reproduces the mechanical equilibrium of the boundaries, and corresponds to the solution of a dislocation-free elastic volume Ω with the boundary conditions $(F_d - F^D)$ and $(U_d - U^D)$ on $\partial\Omega_1$ and $\partial\Omega_2$, respectively.

This decomposition has been applied to the problem of nano-indentation of a crystal by a sphere [5]. The calculation of $((\sigma_{\text{diff}}))$ is solved classically using a finite-element code (CASTEM2000). The plastic displacement U^D from the dislocation motion is computed in the following manner: the space is divided in small subvolumes V containing the node of the meshed surface where the displacement must be established. Then on each node, the distortion β^p is obtained by

$$\beta^p = \frac{\mathrm{d}A \cdot b}{V}$$

where $\mathrm{d}A$ is the swept area of a moving dislocation. This discrete plastic field of distortion is transformed in continuous plastic field via Gaussian distribution functions f

$$U^D = \int f(\beta^p) \cdot \mathrm{d}X.$$

5. Applications

5.1. Bulk deformation of crystal

The initial configuration for this type of simulation consists of a random distribution of segments pinned at their end (figure 10(a)). The initial multiplication mechanism is based on Frank Read source activation as in real crystals, where lines of dislocations are pinned at their ends on fix obstacles (sessile dislocations, vacancy, ...) (figure 10(b)). This initial configuration is not initially under mechanical equilibrium, but during the first simulation steps, because the whole contribution of dislocations is computed when displacing a segment the structure relaxes by forming 3D loops (cross-slip mechanism). Moreover, the pinned point effect is thought to become negligible when the dislocation density is high enough.
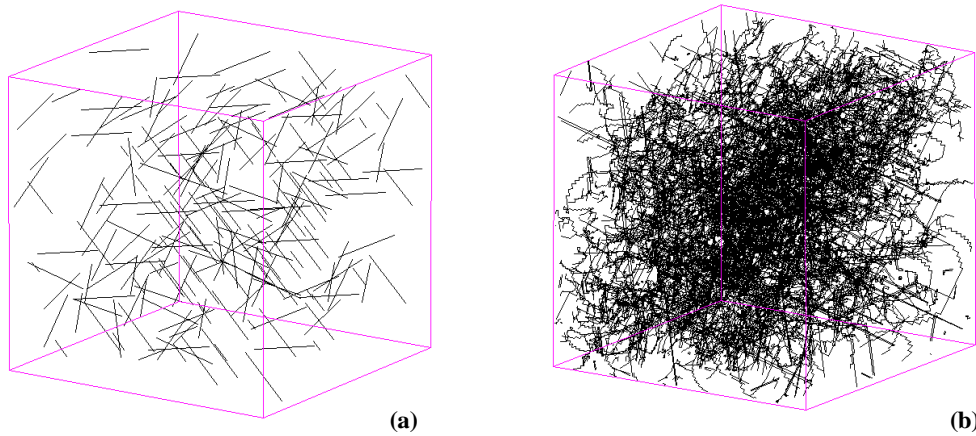

(a) **(b)**

Figure 10. (a) Example of an initial configuration of segments. (b) Frank Read multiplication mechanism.

To study the characteristic of self organization patterns of a dislocation population, the crystal is pulled in tension at a constant strain rate, typically $\mathrm{d}\varepsilon/\mathrm{d}t = 50\ \mathrm{s}^{-1}$. The tensile axis
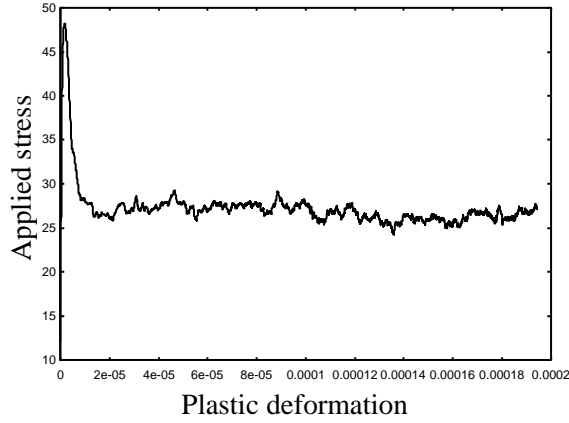
Figure 11. (σ, ε) curve, $d\varepsilon/dt = 50$ s^{-1}.
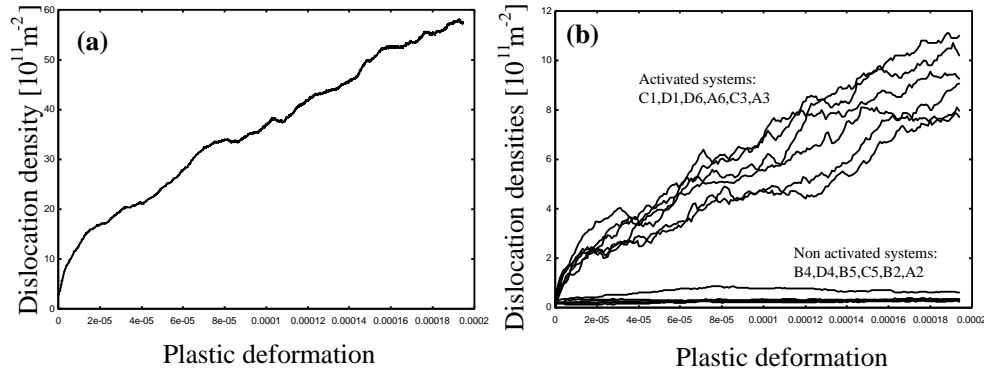

Figure 12. Density dislocation evolution against the plastic strain. (a) Total density; (b) Dislocation density on each slip system (Schmid and Boas notation).

is chosen along a crystallographic direction such as [100] or [111], that allows to activate several slip systems. The strain rate used is in the range of quasi-static testing, avoiding dynamic testing ($d\varepsilon/dt > 100$ s^{-1}) conditions, where plastic deformation is localized on a reduced number of slip systems.

Typical stress-strain curves are shown in figure 11. The initial transient peak in figure 11 is caused by an artifact related by the initial configuration: there is initially a too low mobile dislocation density which is unable to achieve the imposed strain rate because the pinned segments sources have not been activated. In cases where the initial configuration has a higher density of dislocations which can accommodate more rapidly the strain rate, the transient peak is absent.

During deformation, the dislocations density continuously increases as shown in figure 12(a), and the repartition on each slip system, figure 12(b), is in agreement with their respective Schmid factor. Moreover, the homogenous repartition of dislocations among the activated slip systems ensures that the strain rate used is well in a quasi-static domain of deformation [18].

The microstructure of the deformed state are shown in figure 13, where a thin slice is cut through the simulated cube. One can observe the emergence of tangled dislocation
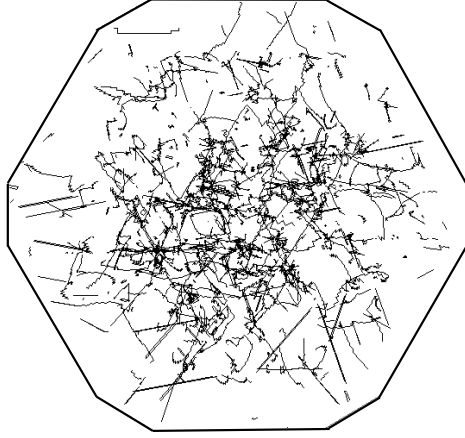
Figure 13. Cut of a 1 μm [111] thick slice within the simulated structure, $\varepsilon = 2 \times 10^{-4}$.

walls, which are thought to be the initiation of the cell structure developed at higher strain. However, the actual limit of the simulation (due to the N^2 algorithm) prevents us getting higher strain than $\varepsilon = 0.05\%$ in reasonable computing time.

5.2. Free surface

To illustrate the importance of the image forces from a free surface, the evolution of the image forces tensor components are calculated as a function of the depth in the cube, figure 14(a). The dislocation configuration in the cube has a dislocation density $\rho = 2 \times 10^{12}$ m^{-2}, and the Boussinesq method has been applied using a mesh of 17 948 points on one surface of the cube. The image forces significantly affect the volume to a depth of 4 μm. However, if one compares the magnitude the image force field and the dislocation direct stress field, both resolved on a slip system, it appears that the effect of the former affect the volume to a depth of 2 μm, figure 14(b).

5.3. Nano-indentation test

The principle of the nano-indentation test is to impose the Hertzian elastic stress field corresponding to the contact of a sphere on a flat surface. As observed experimentally, dislocation loops are nucleated under the indenter. These loops must be nucleated when either a macroscopic or a microscopic loading criterion is satisfied. The local criterion refers to the critical resolved shear stress on the slip planes for loop nucleation. However, this value is not very well known yet due to the high complexity of the atomistic distortions involved under sharp indenters. Since the macroscopic load is decreased when a new loop is introduced in the crystal, an alternative scheme consists in matching the computed applied load with the appropriate experimental data, i.e. the nano-indentation loading curve on pure single crystals. This criterion is the one used in this paper. This preliminary experiment is necessary to run the simulation with some physical parameter. In future, the critical shear stress for loop nucleation will be fixed and the simulation will be executed without any experimental parameter.

Dislocation loops are nucleated as prismatic loops under the indenter at the locus of maximum shear stress. The area of the nucleated loop is equal to the projected contact area
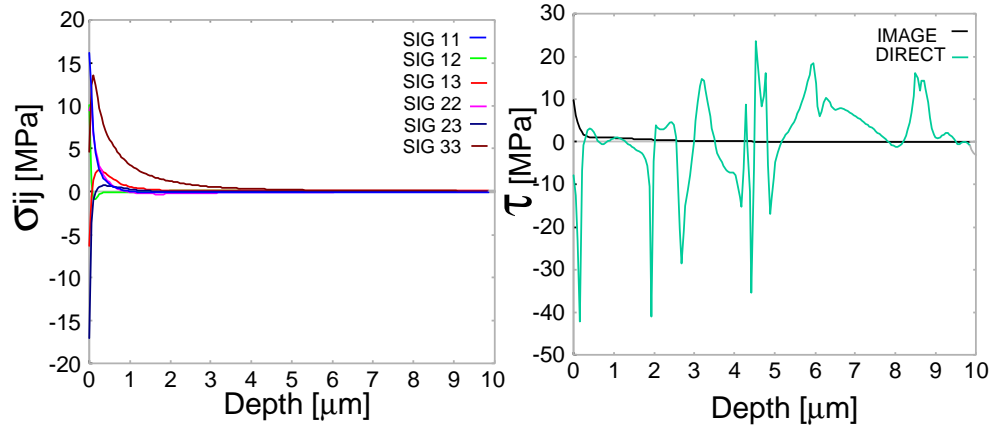
Figure 14. (a) Evolution of the six components of the image force tensor against the depth in the cube from the surface. Cube with a dislocation density $\rho = 2 \times 10^{12}$ m^{-2}. (b) Comparison of image forces and direct dislocation stress fields resolved on $(11\bar{1})$ $[\bar{1}10]$.
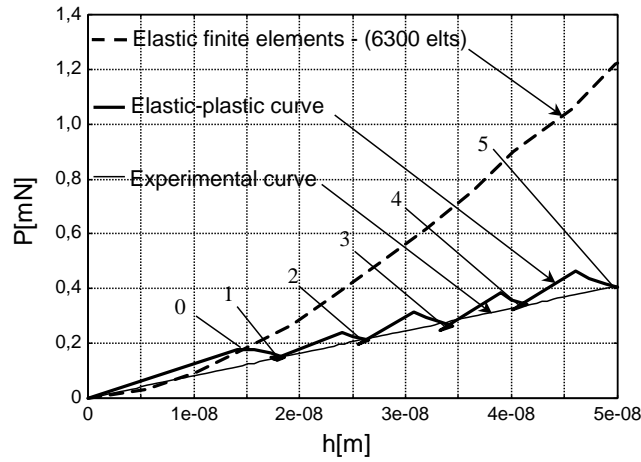

Figure 15. Load displacement curve in the case of a 50 nm [001] indentation.

of the indenter [19]. To obtain this shear stress threshold, prismatic loops are nucleated until the macroscopic force applied on the indenter is equal to that measured experimentally on a load-displacement (P–h) curve obtained on pure Cu. Figure 15 displays an example of such an adjustment in the case of a [001] indentation on Cu to a depth of 50 nm. The initial solution (point 0 on figure 15) is given by the Hertzian solution as calculated by the finite-element code, then nucleations of loops decrease the macroscopic force P until it reaches the experimental curve (point 1). Dislocations then move under the heterogeneous stress field taking into account the boundary conditions. When the dislocation strain becomes negligible, this relaxation process is stopped and an load increment is applied. This scheme is repeated during the indentation process (points 1–5). This procedure ensures the loading process to be quasi-static. The dislocation microstructures corresponding to depths of 15, 19, 35 and 50 nm (points 0, 1, 3 and 5, figure 15) are shown on figure 16.
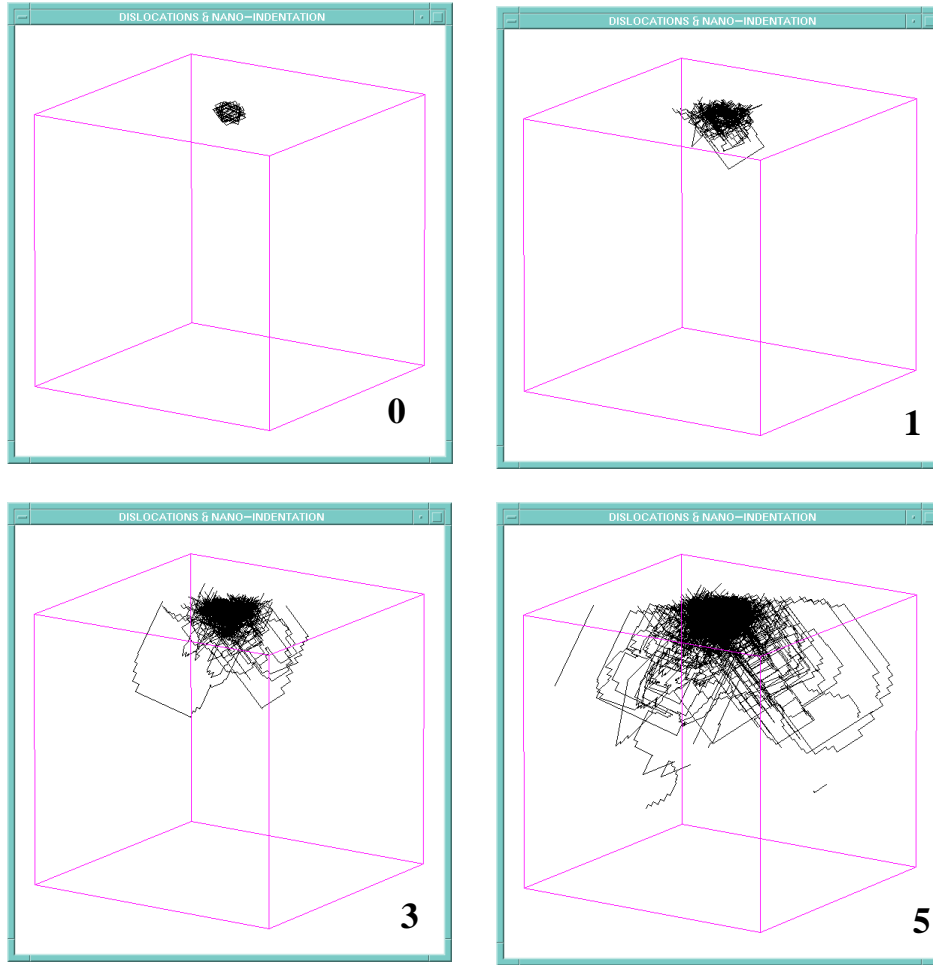
Figure 16. Indent induced dislocation microstructure corresponding to figure 15.

The simulated microstructure has been directly compared to that obtained from transmission electron microscope observations as a result of an accurate modelling of the experimental procedure (reset of the indenter load, cut of a thin slice in the cube, relaxation due to image forces on both sides of the foil) [19].

6. Conclusion

This papers reviews the different techniques used in the simulation of dislocation dynamics in fcc metals on a mesoscopic scale. New acceleration methods for the long-distance stress calculation have been implemented. Boundary conditions have been solved for different cases (bulk, thin film, indentation). Solving complex boundary condition problems requires coupling between the mesoscopic code and the finite-element approach.

Future developments concern an extension of this coupling in order to take into account plastic displacements at interfaces to simulate, for example, the unloading part of the indentation process and the plastic behaviour of films on substrate and of multilayers.

Acknowledgments

The authors would like to thank CNRS-GdR 1165 'Simulations numériques et modélisations mésoscopiques en métallurgie' for supporting this work, the French-Hungarian exchange program Balaton and the Edinburgh Parallel Computer Centre (EPCC) for the use of their machine. We also wish to thank LAMS/DMT of CEA Saclay for providing the finite-element code CASTEM 2000.

References

[1] Kubin L P, Canova G, Condat M, Devincre B, Pontikis V and Bréchet Y 1992 *Solid State Phenomena* **23&24** 455
[2] Devincre B and Kubin L P 1997 *Mater. Sci. Eng.* A **234–236** 8
[3] Verdier M 1996 *PhD Thesis* INP, Grenoble
[4] Fivel M 1997 *PhD Thesis* INP, Grenoble
[5] Fivel M, Verdier M and Canova G 1997 *Mater. Sci. Eng.* A **234–236** 923
[6] Fivel M C, Gosling T J and Canova G R 1996 *Modelling Simulation Mater. Sci. Eng.* **4** 581
[7] Essmann U and Mughrabi H 1979 *Phil. Mag.* A **40** 731
[8] Devincre B and Condat M 1992 *Acta Metall Mater.* **40** 2629
[9] De Wit R 1967 *Phys. Status Solidi* **20** 575
[10] Cottrell A H 1964 *Theory of Crystal Dislocations* (London: Blackie and Son)
[11] Mughrabi H 1973 *Proc. of the 3rd Int. Conf. on the Strength of Metals and Allloys (ICSMA3)* vol 1 (Cambridge: Cambridge Institute of Metals) p 407
[12] Alshits V I and Indenbom V L 1979 *Dislocations in Solids* vol 7, ed F R N Nabarro (Amsterdam: North-Holland) p 43
[13] Bonneville J, Escaig B and Martin J L 1988 *Acta Metall.* **36** 1989
[14] Devincre B and Kubin L P 1994 *Modelling Simulation Mater. Sci. Eng.* **2** 559
[15] van-der-Giessen E and Needleman A 1995 *Modelling Simulation Mater. Sci. Eng.* **3** 689
[16] Boussinesq J 1885 *Applications des potentiels à l'étude de l'équilibre et du mouvement des solides élastiques* (Paris: Gauthier-Villars)
[17] Gosling T J and Willis J R 1993 *J. Mech. Phys. Solids* **42** 1199
[18] Devincre B and Kubin L P 1997 *Phil. Trans. R. Soc.* A **355** 2003
[19] Fivel M C, Robertson C F, Canova G R and Boulanger L *Acta Mater.* to be published